

## Identifying TeV Source Candidates among *Fermi*-LAT Unclassified Blazars

G. CHIARO,<sup>1</sup> M. MEYER,<sup>2</sup> M. DI MAURO,<sup>3</sup> D. SALVETTI,<sup>1</sup> G. LA MURA,<sup>4</sup> AND D. J. THOMPSON<sup>3</sup>

<sup>1</sup>*Institute of Space Astrophysics & Cosmic Physics, INAF  
Via Bassini 15, I-20133 Milano Italy*

<sup>2</sup>*Kavli Institute for Particle Astrophysics and Cosmology, Dpt. of Physics, SLAC,  
Stanford University, Stanford, California 94305, USA*

<sup>3</sup>*NASA Goddard Space Flight Center  
Greenbelt, MD 20771 USA*

<sup>4</sup>*Lab. de Instrumentacao e Fisica Experimental de Particulas. LIP  
Av. Gama Pinto 2, Lisboa, Portugal*

(Received July, 2019)

Submitted to ApJ

### ABSTRACT

Blazars and in particular the subclass of high synchrotron peaked Active Galactic Nuclei are among the main targets for the present generation of Imaging Atmospheric Cherenkov Telescopes (IACTs) and will remain of great importance for very high-energy  $\gamma$ -ray science in the era of the Cherenkov Telescope Array (CTA). Observations by IACTs, which have relatively small fields of view ( $\sim$  few degrees), are limited by viewing conditions; therefore, it is important to select the most promising targets in order to increase the number of detections. The aim of this paper is to search for unclassified blazars among known  $\gamma$ -ray sources from the *Fermi* Large Area Telescope (LAT) third source catalog that are likely detectable with IACTs or CTA. We use an artificial neural network algorithm and updated analysis of *Fermi*-LAT data. We found 80  $\gamma$ -ray source candidates, and for the highest-confidence candidates, we calculate their potential detectability with IACTs and CTA based on an extrapolation of their energy spectra. Follow-up observations of our source candidates could significantly increase the current TeV source population sample and could ultimately confirm the efficiency of our algorithm to select TeV sources.

*Keywords:* gamma rays — blazars — catalogs — surveys

### 1. INTRODUCTION

Blazars, some of the most powerful Active Galactic Nuclei (AGNs), have a relativistic jet pointing toward the observer (e.g., [Abdo et al. 2010](#); [Massaro et al. 2015](#)) and show rapid variability and high optical and radio polarization. Such objects are the most numerous class of extragalactic sources detected by TeV telescopes, the most sensitive of which are the Imaging Atmospheric Cherenkov Telescopes (IACTs) such as MAGIC<sup>1</sup>, H.E.S.S.<sup>2</sup>, VERITAS<sup>3</sup>, and the upcoming Cherenkov Telescope Array (CTA)<sup>4</sup>. Despite their high sensitivity, however, observations by current IACTs are limited by their fairly small fields of view ( $\sim$  few degrees), weather conditions, the need for relatively dark night skies, and by a high background that requires fairly long observations. A source with a flux of  $\sim 1\%$  of the Crab Nebula flux requires around 50 hours of observation time for a detection at  $5\sigma$ . IACTs typically take data for only about 1200 hours per year ([De Naurois et al. 2015](#)). Those constraints provide a strong incentive to identify likely targets for IACT observations.

Corresponding author: Graziano Chiaro  
[graziano.chiaro@inaf.it](mailto:graziano.chiaro@inaf.it)

<sup>1</sup> <https://magic.mpp.mpg.de/>

<sup>2</sup> <https://www.mpi-hd.mpg.de/hfm/HESS/>

<sup>3</sup> <https://veritas.sao.arizona.edu/>

<sup>4</sup> <https://www.cta-observatory.org/>

Blazar Spectral Energy Distributions (SEDs) show two broad peaks in a  $\nu f_\nu$  representation. The low-energy peak is attributed to synchrotron radiation, and the high-energy one is usually thought to be produced by inverse Compton radiation (IC) (e.g. Sikora et al. 1994). Based on the position of the synchrotron peak ( $\nu_{peak}^S$ ) in the SED, blazars are divided into three subclasses: low-synchrotron-peaked (LSP, with  $\nu_{peak}^S \leq 10^{14}$  Hz), intermediate-synchrotron-peaked (ISP, with  $10^{14}$  Hz  $< \nu_{peak}^S \leq 10^{15}$  Hz) and high-synchrotron-peaked (HSP, with  $\nu_{peak}^S > 10^{15}$  Hz) (Abdo et al. 2010). HSPs, primarily BL Lac objects, represent the most numerous class of extragalactic TeV-energy sources. The TeVCat<sup>5</sup> is an online, interactive catalog for very-high-energy (VHE energies,  $E > 100$  GeV)  $\gamma$ -ray astronomy (Horan et al. 2008). This catalog reports 223 TeV sources as of this writing. Among the 61 objects associated with blazars, 51 of them are HSPs and only 10 are LSP/ISP flat-spectrum radio quasars (FSRQs)<sup>6</sup>.

All-sky observations with the Large Area Telescope (LAT) on board the Fermi Gamma-ray Space Telescope (Fermi) (Atwood et al. 2009) at GeV energies offer opportunities to find such targets. An example is the Third Catalog of Hard *Fermi*-LAT Sources (3FHL: Ajello et al. 2017), which reports the locations and spectra of sources significantly detected in the 10 GeV - 2 TeV energy range during the first 7 years of the *Fermi* mission. From the 3FHL it is possible to select TeV candidates by  $\gamma$ -ray flux and photon index.

An alternative approach to searching for TeV candidates is to find objects belonging to a class of sources likely to be seen at TeV energies. In the case of blazars, this can be done by identifying those objects whose synchrotron emission peaks at high frequencies. An example of this approach is the second *WISE* High Synchrotron Peak Catalog (2WHSP) (Chang et al. 2017), which is a list of HSP candidates based on multi-frequency analysis of  $\gamma$ -ray source candidates with  $|b| > 10^\circ$ .

Here we present a third approach to search for TeV HSP source candidates. This method includes two steps: (1) we use  $\gamma$ -ray variability information to search out potential HSPs among the unclassified *Fermi*-LAT sources; and (2) we analyze  $\gamma$ -ray spectra of these sources using more *Fermi*-LAT data than used in published catalogs. The starting point is the third *Fermi*-LAT all-sky catalog of sources detected at energies between 100 MeV and 300 GeV (3FGL: Acero et al. 2015). The 3FGL catalog lists 3033  $\gamma$ -ray sources, of which 1745 are AGNs, mostly BL Lacs and FSRQs, and includes  $\gamma$ -ray source locations, energy spectra, variability information on monthly time scales, and likely associations with objects seen at other wavelengths. In this catalog 573 sources are listed as blazars of uncertain type (BCUs) and 1010 objects lack a plausible counterpart at other wavelengths (Unassociated Catalog Sources, UCSs)<sup>7</sup>.

Although BCUs and UCSs often lack optical spectra and sufficient information for a rigorous classification, statistical methods such as the Artificial Neural Network (ANN) algorithm can potentially provide classifications of these sources (e.g., Chiaro et al. 2016; Saz Parkinson et al. 2016; Salvetti et al. 2017; Lefaucheur & Pita 2017). In particular, Saz Parkinson et al. (2016) found 559 of the UCS sources have characteristics similar to those of AGN. These UCS<sub>agns</sub> are combined with the original 573 BCUs from the 3FGL catalog to provide the targets for our search for HSP/TeV candidates.

The paper is organized as follows: in Sect. 2 we present the machine learning method used in this study; in Sect. 3 we describe the selection of HSP candidates among the uncertain 3FGL objects; and in Sect. 4 we discuss the results of a dedicated *Fermi*-LAT analysis of the sources found analyzing 104 months of data. In Sect. 5 we examine the detectability of the targets by the present generation of IACTs and CTA. In Sect. 6 we summarize the conclusions of this study.

## 2. THE ANN SEARCH METHOD

The starting point for selecting HSP candidates is the ANN method previously applied to *Fermi*-LAT sources to distinguish FSRQ-like sources from those with BL Lac characteristics (Chiaro et al. 2016; Salvetti et al. 2017). The key idea is that the  $\gamma$ -ray flares of BL Lacs tend to be smaller and less frequent than those of FSRQs. The input is the empirical cumulative distribution function (ECDF) of monthly  $\gamma$ -ray flux values for each source, taken from the 3FGL. We included in the algorithm values corresponding to increments of 10% from the 10th to the 100th percentile of the ECDF. The algorithm computes a likelihood value arranged to have two possibilities: class *A* or class *B*, with a likelihood ( $L$ ) assigned to each analyzed source so that the likelihoods to belong to one or the other of the two classes are related by  $L_A = 1 - L_B$ . In this way, the greater the value of  $L_A$ , the greater the likelihood that the source is a class *A* candidate. In this case, the likelihood applies to the source having HSP characteristics,  $L_{HSP}$ . This approach

<sup>5</sup> <http://tevcad.uchicago.edu/>

<sup>6</sup> The rest of the sources in TeVCat are Galactic sources or of unidentified nature.

<sup>7</sup> A preliminary version of the 4FGL catalog is available at [https://fermi.gsfc.nasa.gov/ssc/data/access/lat/8yr\\_catalog/](https://fermi.gsfc.nasa.gov/ssc/data/access/lat/8yr_catalog/), but it does not include the variability information needed for this analysis.

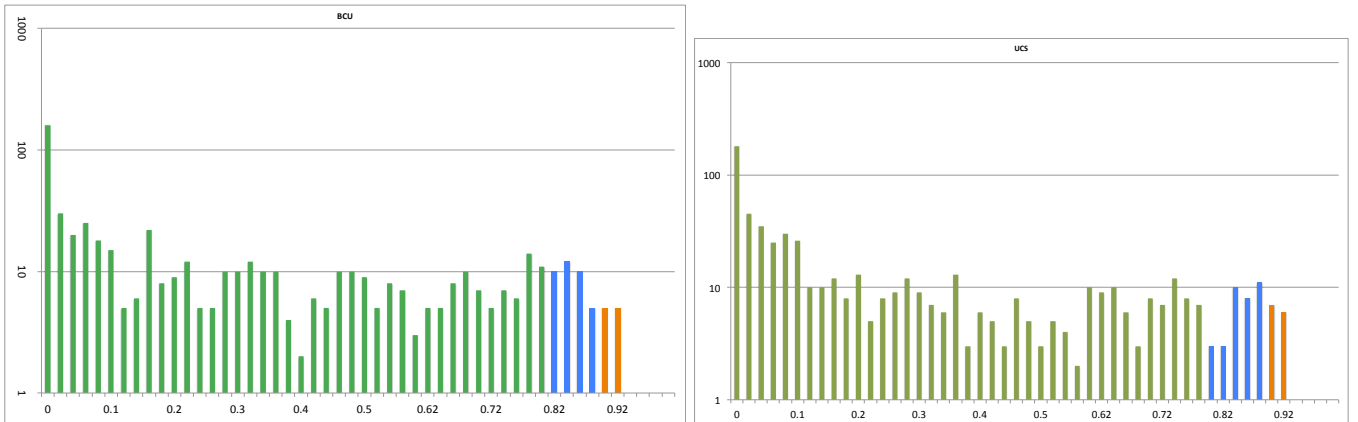


**Figure 1.** ANN likelihood to be HSP candidates of 3FGL BCUs (left) and  $UCS_{agn}$  (right). Blue bars: sources with  $0.89 > L_{HSP} > 0.8$ ; Red bars: VHC candidates with  $L_{HSP} > 0.89$

uses the two-layer-perceptron ANN technique (Gish 1990; Bishop 1995), which is probably the most widely used architecture for practical applications of neural networks. Data enter the neural network through nodes in the input layer. The information travels across the links and is processed in the nodes through an activation function. Each node in the output layer returns the likelihood of a source to be a specific class. We applied the algorithm to the three synchrotron peak subclasses as classified in the Third Catalog of Active Galactic Nuclei detected by the *Fermi* LAT (3LAC; Ackermann et al. 2015) in order to train it to distinguish each source class.

Repeating the analysis of Chiaro et al. (2016) as a cross-check on that analysis, we considered 289 HSPs and 824 non-HSP objects classified in the third *Fermi*-LAT AGN catalog (3LAC; Ackermann et al. 2015). Maintaining the same ratio as in the catalog, that is, one third HSPs and two thirds non-HSP sources, we randomly mixed the sample and divided it into 3 subsamples: training, validation, and testing. The training sample is used to optimize the network. The validation sample is used to avoid over-fitting. The testing sample is independent both of the training and validation ones and was used to monitor the accuracy of the network. Although the random sampling resulted in a different training set from the previous analysis, the results were the same: for  $L_{HSP} > 0.8$ , 75% of the sources have characteristics of HSPs, while for  $L_{HSP} > 0.89$ , we expect 90% of the sources to be HSP-like.

### 3. IDENTIFYING HSP CANDIDATES

We then applied the ANN HSP algorithm to the 573 BCUs and the 559  $UCS_{agn}$  of our sample. The resulting likelihood distributions plotted in Fig. 1 show, as expected, a peak at  $L_{HSP} = 0.0$  due to the non-HSP populations (ISP and LSP), which are much more numerous than HSPs at energies covered by the *Fermi* LAT. As for the original analysis (Chiaro et al. 2016), the lack of a peak at  $L_{HSP} = 1.0$  indicates that the ANN network was not able to separate HSPs cleanly, but for the purpose of selecting candidates for additional analysis we are primarily interested in finding a high fraction of the sources with the desired characteristics. Requiring the  $L_{HSP} > 0.8$  value, we identified 48 BCU and 32  $UCS_{agn}$  as HSP candidates. Applying the higher threshold value  $L_{HSP} > 0.89$ , we identified 11 BCUs and 5  $UCS_{agn}$  as Very High Confidence (VHC) HSP candidates. Table 1 and Table 2 show the full lists of candidates. The names of the VHC candidates are shown in bold.

We compared the results of our analysis with the list of blazars presented in the 2WHSP catalog (Chang et al. 2017), since both methods attempt to identify HSP objects. Of the 11 VHC candidates from the BCU list, 6 were also identified by 2WHSP: 3FGL J0506.9–5435, 3FGL J0921.0–2258, 3FGL J1155.4–3417, 3FGL J1711.6+8846, 3FGL J1714.1–2029, and 3FGL J1944.1–4523. None of the 5 VHC candidates from the UCS list were found in the 2WHSP catalog. Similar fractions were found for the other parts of the lists, indicating that the two methods are complementary in finding candidate HSPs.

### 4. FERMI-LAT SPECTRAL ANALYSIS

Because the 4FGL catalog will soon be available with a larger sample of sources to study, we chose to focus our spectral analysis for this new method of selecting HSP candidates on the 16 VHC sources. We analyzed 104 months of *Fermi*-LAT Pass 8 (Atwood et al. 2013) data from 2008 August 4 to 2017 April 4, selecting  $\gamma$ -ray events in the

energy range  $E = [0.1, 1000]$  GeV, passing standard data quality selection criteria and zenith angle cuts for AGN (e.g. Meyer et al. 2019), in order to find the  $\gamma$ -ray properties of our HSP candidates. We considered events belonging to the Pass 8 SOURCE event class and used the corresponding instrument response functions P8R2\_SOURCE\_V6, since we were interested in point source detection. We used the interstellar emission model (IEM) released with Pass 8 data (Acero et al. 2016) (i.e., `gll_iem_v06.fits`). This is the model recommended for use with Pass 8 analyses. We also included the standard template for the isotropic emission (`iso_P8R2_SOURCE_V6_v06.txt`)<sup>8</sup>.

We developed an analysis pipeline using FermiPy, a Python package that automates analyses with the *Fermi* Science Tools (Wood et al. 2017)<sup>9</sup>. FermiPy includes tools that can 1) generate simulations of the  $\gamma$ -ray sky, 2) detect point sources, and 3) calculate the characteristics of their SEDs.

The likelihood analysis works on a square region of interest (ROI). We used a  $16^\circ \times 16^\circ$  ROI centered on the sources of our sample. We analyzed each ROI separately. In each ROI, we binned the data with a pixel size of  $0.08^\circ$  and 8 energy bins per decade. Our background model included the IEM, isotropic template and sources from the preliminary 8-year list, FLSY<sup>10</sup>, except for the source being analyzed. We allowed the normalization and slope of the IEM and the normalization of the isotropic template to vary. We first relocalized the source of interest, and then we searched for new point sources with Test Statistic  $TS > 25$ , defined as twice the difference between the log-likelihood for the null hypothesis (no source) and the hypothesis of a source at the location. New sources were then added to the analysis. We then analyzed each of our HSP candidates, assuming a power-law spectrum after determining that all the VHC candidates used that spectral form in the 3FGL catalog (Acero et al. 2015). For the individual energy bins, we plotted as upper limits those points with a  $TS < 9$ .

In Table 1 and Table 2 we report the following parameters for the HSP candidates: the best fit and  $1\sigma$  error of the position, the  $TS$  of detection, the photon index found for a power-law SED shape, the flux, and the value of  $L_{HSP}$ . The photon index parameter, if less than 2, can be a relevant indicator for an IC peak at TeV energies and therefore quite useful in selecting IACT and CTA candidates. The mean and rms of the photon indexes of HSPs are  $1.87 \pm 0.20$  while for LSPs and ISPs these are  $2.21 \pm 0.18$ ,  $2.07 \pm 0.20$  respectively (Ackermann et al. 2015).

We have repeated the analysis with a log-parabola intrinsic spectrum instead of a power law. Only for three sources (3FGL J0921.0-2258, 3FGL J0153.4+7114, and 3FGL J0506.9-5435) did we find that a log-parabola is preferred at the  $4\sigma$  level, i.e.  $TS_{\text{curv}} > 16$ , where  $TS_{\text{curv}}$  is twice the difference of the log-likelihood values of the best fit with a log-parabola and a power law, respectively. These results are largely consistent with the spectral parameters listed in the preliminary 4FGL catalog<sup>11</sup>. The 4FGL sources corresponding to 3FGL J0921.0–2258 and 3FGL J0153.4+7114 have power-law spectra instead of the curved spectra we found, although the evidence for curvature is of low significance in our analysis. If we had used the power-law fit, the extrapolations would have obviously been higher.

## 5. TEV CANDIDATES

In this section, we compare the extrapolated fluxes of the *Fermi*-LAT spectra of our VHC sources to the sensitivity of present IACTs and the future CTA. In the case that the log-parabola fit to the *Fermi*-LAT data is preferred with  $TS_{\text{curv}} > 16$ , we use the log-parabola parametrization for the extrapolation and the best-fit power law otherwise. In order to evaluate whether the VHC HSP candidates can realistically be observed with IACTs or CTA, we must take into account the interaction of  $\gamma$ -rays with photons of the extragalactic background light (EBL). The EBL spans the wavelength regime from ultraviolet to far-infrared wavelengths and mainly consists of the integrated starlight emitted over the history of the Universe and starlight absorbed and re-emitted by dust in galaxies (Hauser et al. 2001; Kashlinsky 2005). During the propagation of  $\gamma$  rays through the EBL, the electron-positron pairs produced via  $\gamma\gamma \rightarrow e^+e^-$  leads to an attenuation of the initial  $\gamma$ -ray flux (Nikisov et al. 1962; Gould & Schreder 1967; Dwek et al. 2013). To properly evaluate the absorption effect of the EBL it is necessary to know the redshift of the analyzed  $\gamma$ -ray source. Since the redshifts of the selected VHC HSP candidates are unknown, we assume redshifts of  $z = 0$  and  $z = 0.5$  for the calculation. These are typical values of observed  $\gamma$ -ray BL Lacs<sup>12</sup>. We use these  $z$  values while acknowledging that the blazar redshift range is a very open and long-standing debate. Some authors argue that the BL Lacs without a redshift are likely much more distant than those with a measured one (e.g., Padovani et al. 2012), so it could be possible that some objects fall beyond the 0.5 redshift.

<sup>8</sup> For descriptions of these templates, see <http://fermi.gsfc.nasa.gov/ssc/data/access/lat/BackgroundModels.html>.

<sup>9</sup> See <http://fermipy.readthedocs.io/en/latest/>.

<sup>10</sup> [https://fermi.gsfc.nasa.gov/ssc/data/access/lat/fl8y/gll\\_psc\\_8year\\_v5.fit](https://fermi.gsfc.nasa.gov/ssc/data/access/lat/fl8y/gll_psc_8year_v5.fit)

<sup>11</sup> [https://fermi.gsfc.nasa.gov/ssc/data/access/lat/8yr\\_catalog/](https://fermi.gsfc.nasa.gov/ssc/data/access/lat/8yr_catalog/)

<sup>12</sup> We recognize that a redshift identically 0 is unrealistic. This choice provides a “best case” limit.

Using the EBL model of [Dominguez et al. \(2011\)](#), we extrapolate the best-fit spectra obtained with the *Fermi*-LAT analysis in Sec. 4 up to 10 TeV with the assumed redshift values. The results are shown in Fig. 2 and Fig. 3 where we compare the extrapolated fluxes with the CTA sensitivity ([Acharyya et al. 2019](#)) for 50 hours (5 hours) of observations as a solid (dashed) gray line. The sensitivities for currently operating IACT arrays H.E.S.S., MAGIC, and VERITAS are shown as a red band ([Holler et al. 2015](#); [Aleksć et al. 2016](#))<sup>13</sup>. The CTA sensitivity curves are available for the northern and southern array and for zenith angles ( $Z$ ) of  $20^\circ$  and  $40^\circ$ . We choose the sensitivity curve depending on the source declination  $\delta$  assuming CTA site locations at  $28.7^\circ$  northern latitude and  $24.7^\circ$  southern latitude. For  $\delta > 58.7^\circ$ , we choose the northern array with  $Z = 40^\circ$ , for  $58.7^\circ \leq \delta < 2.7^\circ$  the northern array with  $Z = 20^\circ$ , for  $2.7 \geq Z \geq -54.7^\circ$  the southern array with  $Z = 20^\circ$ , and the southern array with  $Z = 40^\circ$  for  $\delta < -54.7^\circ$ <sup>14</sup>.

In Table 3, we report an estimate of the maximum redshift values of the VHC TeV candidates so that the sources are still detectable at  $5\sigma$  for 50-hr observations with current IACTs as well as 5- and 50-hr CTA observations. For these estimates, we assume that the spectra are detectable if the extrapolation is above the sensitivity curves. We also report how these values change if the best-fit spectral parameters are changed by their  $1\sigma$  statistical uncertainties. An actual detection will depend on the spectral shape and the exact exposure time, and therefore these numbers should be regarded as a rough estimate. If no value is given, the source might not be significantly detected with the assumed observation within the assumed redshift range.

Any of the VHC sources that lie at low redshift should be detectable with CTA, with the exception of 3FGL J0921.0–2258, which shows strong intrinsic curvature. Similarly, most sources should already be detectable by the present-generation IACTs if their redshifts are close to 0. For a redshift of  $z = 0.5$ , most sources appear to be good candidates for detection with 50 hours of CTA observations, primarily in the 100-GeV energy range. Only 3FGL J1714.1–2029 seems possible as a candidate for current IACTs if its distance is at the upper end of the range considered, due to the EBL attenuation.

## 6. CONCLUSIONS

Motivated to expand the sample of TeV sources, we applied a machine learning algorithm to variability parameters of *Fermi*-LAT blazar-like sources without firm identifications combined with new analysis of the LAT data for these sources. Follow-up work will require additional multiwavelength studies, including finding redshifts for most of the candidates and targeted observation by IACTs. We also recognize that this search is necessarily incomplete because of the difficulty to distinguish the blazar subclasses by the  $\gamma$ -ray flux properties only. As already pointed out by [Ackermann et al. \(2015\)](#), the  $\gamma$ -ray sources with unknown properties are generally fainter than the well-defined classes. The fainter sources offer less of the flaring information needed for the machine learning method, and so there may be HSP blazars among the sample of 3FGL sources rejected in the first step of our method. The level of incompleteness is difficult to quantify due to the very similar values of the synchrotron peaks of the three blazar subclasses. Nevertheless, some VHC HSP candidates, also thanks to the analysis of *Fermi*-LAT data, are convincing as TeV candidates and should be promising targets for currently operating IACTs, especially if the sources are located below redshifts of  $\sim 0.1$ . If the sources are further away, CTA should be capable of significantly detecting them.

The *Fermi* LAT Collaboration acknowledges generous ongoing support from a number of agencies and institutes that have supported both the development and the operation of the LAT as well as scientific data analysis. These include the National Aeronautics and Space Administration and the Department of Energy in the United States, the Commissariat à l’Energie Atomique and the Centre National de la Recherche Scientifique / Institut National de Physique Nucléaire et de Physique des Particules in France, the Agenzia Spaziale Italiana and the Istituto Nazionale di Fisica Nucleare in Italy, the Ministry of Education, Culture, Sports, Science and Technology (MEXT), High Energy Accelerator Research Organization (KEK) and Japan Aerospace Exploration Agency (JAXA) in Japan, and the K. A. Wallenberg Foundation, the Swedish Research Council and the Swedish National Space Board in Sweden. Additional support for science analysis during the operations phase is gratefully acknowledged from the Istituto Nazionale di Astrofisica in Italy and the Centre National d’Études Spatiales in France. This work performed in part under DOE Contract DE-AC02-76SF00515.

<sup>13</sup> The VERITAS sensitivity curve from <https://veritas.sao.arizona.edu/about-veritas-mainmenu-81/veritas-specifications-mainmenu-111> is used.

<sup>14</sup> The sensitivity curves of the northern and southern array are available at [www.cta-observatory.org](http://www.cta-observatory.org)



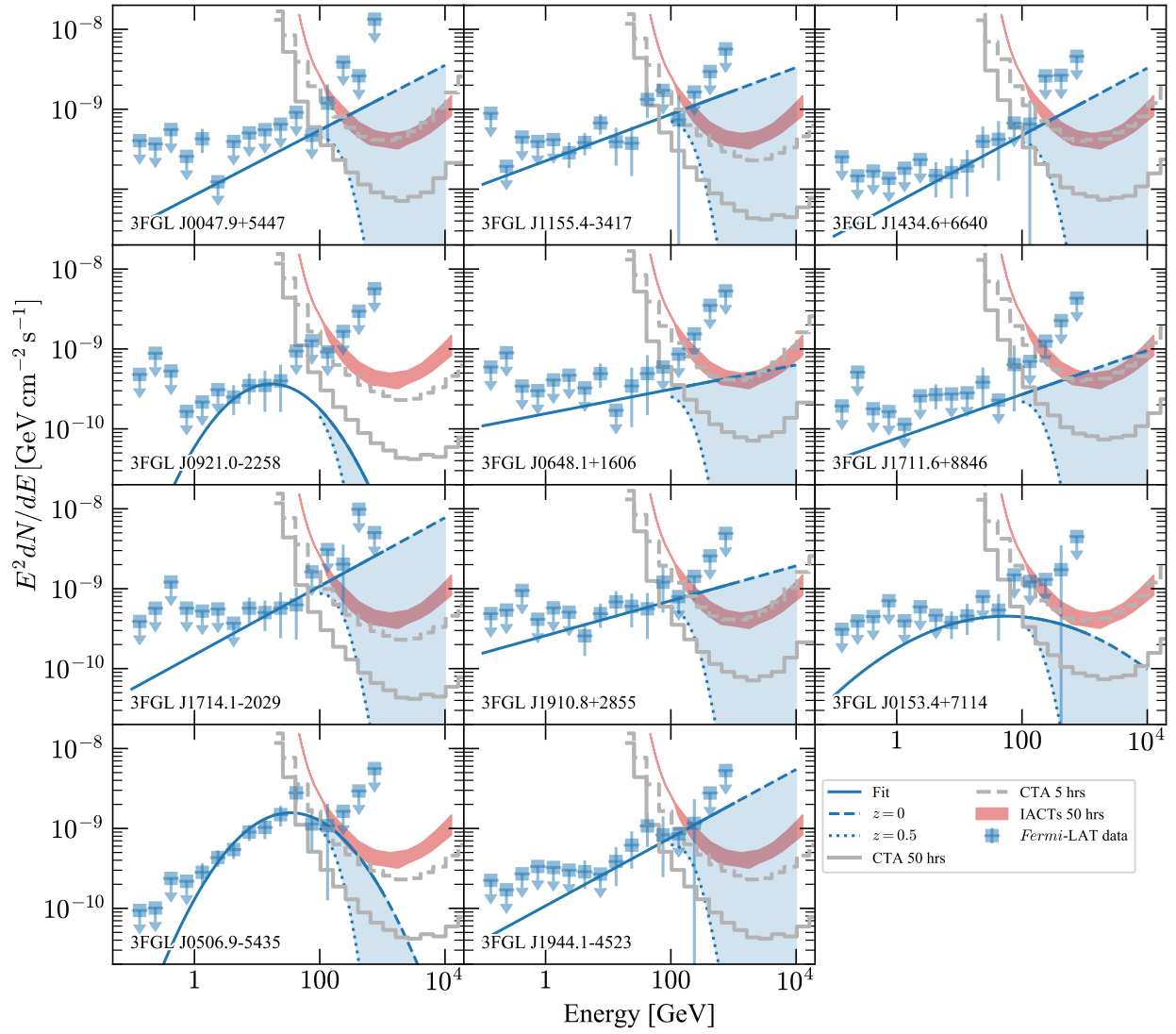


**Figure 2.** SEDs of the VHC BCU sources as TeV candidates. The dashed (dotted) line denotes the extrapolation of the best-fit *Fermi*-LAT spectra up to 10 TeV for a redshift of  $z = 0$  ( $z = 0.5$ ). The shaded region indicates the possible source flux for redshifts between  $0 < z \leq 0.5$ . The CTA sensitivity for 5 (50) hours of observation is shown as a gray dashed (solid) line. The sensitivity curve for either the northern or southern array is used as described in the main text. The 50 hour sensitivity for currently operating IACTs is shown as a red shaded band.

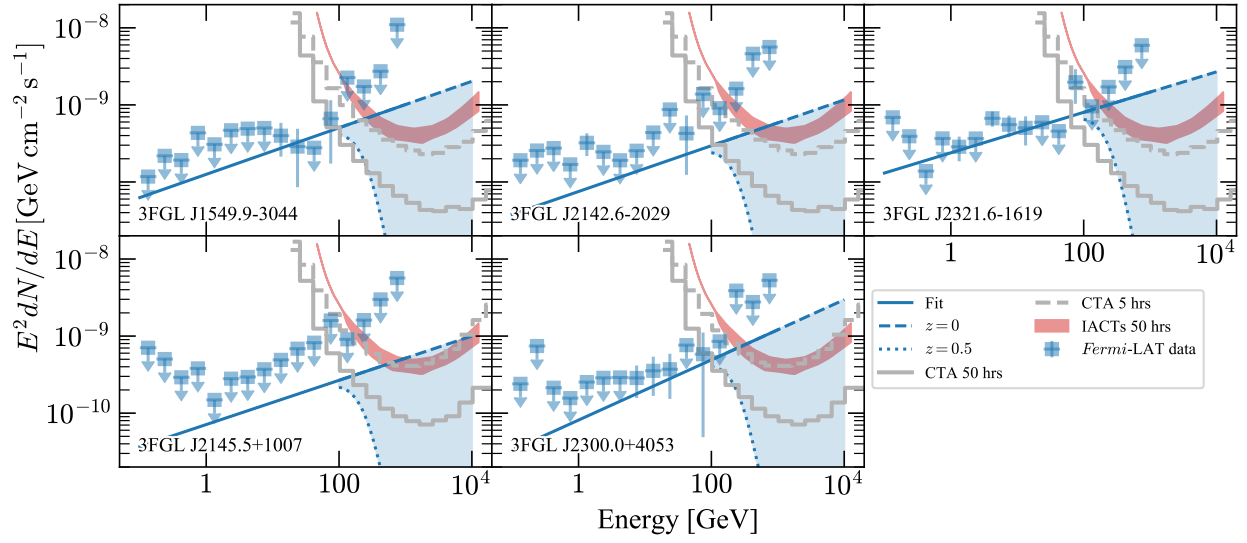


**Figure 3.** SEDs of the VHC UCS sources as TeV candidates. The dashed (dotted) line denotes the extrapolation of the best-fit *Fermi*-LAT spectra up to 10 TeV for a redshift of  $z = 0$  ( $z = 0.5$ ). The shaded region indicates the possible source flux for redshifts between  $0 < z \leq 0.5$ . The CTA sensitivity for 5 (50) hours of observation is shown as a gray dashed (solid) line. The sensitivity curves for either the northern or southern array is used as described in the main text. The 50 hour sensitivity for currently operating IACTs is shown as a red shaded band.

MDM acknowledges support by the NASA *Fermi* Guest Investigator Program 2014 through the *Fermi* multi-year Large Program No. 81303 (P.I. E. Charles) and by the NASA *Fermi* Guest Investigator Program 2016 through the *Fermi* one-year Program No. 91245 (P.I. M. Di Mauro).

This paper has gone through internal review by the CTA Consortium. This research has made use of the CTA instrument response functions provided by the CTA Consortium and Observatory, see <http://www.cta-observatory.org/science/cta-performance/> (version prod3b-v1) for more details.

*Facilities:* *Fermi*, H.E.S.S., MAGIC, VERITAS, CTA

## REFERENCES

- Abdo A.A. , Ackermann M., Agudo I. et al., 2010, ApJ, 716,30
- Acero F., Ackermann, M., Ajello M. et al. , 2015, ApJS, 218, 23
- Acero F., Ackermann, M., Ajello M. et al., 2016, ApJS 223, 26
- Acharyya A., Agudo I., Angüiner E., et al., 2019, Astroparticle Physics, 111, 35-53
- Ackermann, M., Ajello, M., Atwood W.B. et al., 2015, ApJ 810, 14, 34
- Ajello M., Atwood W. B., Baldini L. et al., 2017, ApJS, 232, 18
- Aleksć J., Ansoldi S., Antonelli L. A., et al., 2016, Astroparticle Physics, 72, 76-94
- Atwood W. B. , Abdo A. A., Ackermann M. et al., 2009, ApJ, 697, 1071
- Atwood, W., Albert, A., Baldini, L., et al. 2013, eConf C121028, 8, in Proc. 4th Fermi Symposium, Monterey
- Bishop C.M., Neural Network for Pattern Recognition, 1995
- Chang Y.L. , Arsioli B., Giommi P. et al., 2017, A&A , 598, 17
- Chiaro G. , D.Salvetti, G. La Mura et al., 2016 MNRAS 462.3.3180C
- De Naurois M, Rolland L., 2009, Aph, 32, 331
- Dwek E. , Krennrich F., 2013, APh, 43,112
- Dominguez A., Primack J. R.; Rosario D. J. et al.,2011, MNRAS, 410, 2556
- Gish H., 1990, Proceeding on Acoustic Speech and Signal Processing, p. 1361
- Gould R., Schreder G., 1967, Ph Rv, 155, 1408
- Hauser M., Dwek E. , 2001, ARAA, 39,249
- Holler M., Balzer A., Chalmé-Calvet R., et al., 2015, ArXiv:1509.02896
- Horan D., Wakeley S., 2008, AAS, HEAD meeting 10, id.41.06
- Kashlinsky A., 2005, PhR 409,361
- Lefaucheur J., Pita S. 2007, A&A, 602,86
- Massaro F. , Landoni R. D’Abrusco D. et al., 2015,A&A, 24, 2
- Meyer, M., Scargle, J. D., Blandford, R. 2019, ApJ, in press
- Nikisov A., 1962, Sov.Phys., 14, 393
- Padovani P., Giommi P., Rau A., 2012, MNRAS, 422, 48
- Saz Parkinson P., Xu H., Yu P. et al., 2016, ApJ, 820,2
- Salvetti D. Chiaro G. , La Mura G. et al., 2017, MNRAS, 470, 1291
- Sikora, M., Begelman, M. C., Rees, M. J., 1994, ApJ, 421, 153
- Wood M., Caputo R., Charles E. et al., 2017, ArXiv: 1707.09551



**Table 1.** Results of the *Fermi*-LAT analysis of the full list of BCU HSP candidates. Names of the high-confidence sources are shown in **bold**. Columns: (1) Source name; (2) RA; (3) DEC; (4) 68% error on the position  $\theta$ ; (5) Detection TS 0.1– 300 GeV; (6) Photon Index; (7) Integrated flux in the energy range 0.1– 300 GeV; 8)  $L_{HSP}$ , likelihood the source is an HSP

Source name	RA	DEC	$\theta_{68\%}$	TS	Ph.Index	Flux	$L_{HSP}$
	[deg]	[deg]	[deg]			[ $10^{-9}$ ph/cm <sup>2</sup> /s]	
3FGL J0030.2–1646	7.59	-16.82	0.02	168.7	1.66 ± 0.08	13.4 ± 3.3	0.80
3FGL J0039.0–2218	9.77	-22.32	0.03	89.3	1.67 ± 0.11	9.2 ± 2.9	0.86
3FGL J0040.3+4049	10.09	40.83	0.03	75.9	1.92 ± 0.16	18.2 ± 9.4	0.87
3FGL J0043.5–0444	10.88	-4.72	0.04	54.0	1.91 ± 0.15	16.2 ± 7.2	0.83
3FGL J0043.7–1117	10.94	-11.31	0.04	69.4	1.86 ± 0.12	16.0 ± 5.3	0.88
<b>3FGL J0047.9+5447</b>	12.02	54.81	0.03	56.7	1.58 ± 0.17	4.9 ± 3.2	0.92
3FGL J0132.5–0802	23.19	-8.07	0.03	71.9	1.87 ± 0.11	16.8 ± 5.4	0.84
<b>3FGL J0153.4+7114</b>	28.43	71.26	0.02	80.9	1.82 ± 0.13	17.5 ± 7.3	0.89
3FGL J0204.2+2420	31.09	24.27	0.04	27.6	1.70 ± 0.16	4.7 ± 2.6	0.81
3FGL J0305.2–1607	46.29	-16.14	0.02	147.6	1.80 ± 0.11	17.8 ± 5.8	0.86
3FGL J0342.6–3006	55.71	-30.11	0.04	43.2	1.96 ± 0.14	12.5 ± 4.7	0.84
3FGL J0439.6–3159	69.85	-32.03	0.03	119.9	1.75 ± 0.09	13.3 ± 3.9	0.81
<b>3FGL J0506.9–5435</b>	76.76	-54.60	0.01	455.4	1.50 ± 0.05	14.2 ± 2.2	0.89
3FGL J0515.5–0123	78.87	-1.42	0.04	45.7	1.80 ± 0.11	11.4 ± 4.4	0.85
3FGL J0528.3+1815	82.11	18.27	0.04	35.7	1.67 ± 0.15	6.6 ± 3.6	0.87
3FGL J0620.4+2644	95.17	26.74	0.02	92.0	1.54 ± 0.11	6.3 ± 2.8	0.85
3FGL J0640.0–1252	100.01	-12.90	0.02	174.1	1.52 ± 0.09	10.3 ± 3.4	0.85
3FGL J0646.4–5452	101.62	-54.92	0.03	190.3	1.46 ± 0.29	8.8 ± 1.8	0.87
<b>3FGL J0648.1+1606</b>	102.03	16.09	0.03	40.1	1.82 ± 0.16	10.7 ± 5.9	0.90
3FGL J0650.5+2055	102.64	20.93	0.02	206.2	1.72 ± 0.08	21.9 ± 5.7	0.82
3FGL J0733.5+5153	113.35	51.86	0.03	104.3	1.69 ± 0.10	9.9 ± 3.2	0.85
3FGL J0742.4–8133c	115.45	-81.54	0.05	32.3	2.03 ± 0.28	21.1 ± 15.4	0.88
3FGL J0746.9+8511	117.25	85.22	0.03	119.0	1.68 ± 0.09	10.0 ± 2.8	0.83
<b>3FGL J0921.0–2258</b>	140.24	-22.95	0.03	62.5	1.74 ± 0.14	9.4 ± 4.1	0.91
3FGL J1040.8+1342	160.26	13.72	0.03	69.1	1.71 ± 0.13	8.3 ± 3.4	0.86
3FGL J1141.2+6805	175.33	68.08	0.02	140.1	1.69 ± 0.09	10.9 ± 2.8	0.85
<b>3FGL J1155.4–3417</b>	178.87	-34.33	0.02	147.3	1.64 ± 0.09	11.8 ± 3.3	0.92
3FGL J1158.9+0818	179.71	8.31	0.04	51.5	1.81 ± 0.14	11.0 ± 4.6	0.80
3FGL J1203.5–3925	180.85	-39.42	0.03	103.2	1.70 ± 0.10	13.5 ± 4.5	0.85
3FGL J1319.6+7759	199.95	78.01	0.02	182.6	1.95 ± 0.8	28.3 ± 5.9	0.82
<b>3FGL J1434.6+6640</b>	218.72	66.67	0.03	73.9	1.58 ± 0.12	4.4 ± 1.7	0.92
3FGL J1446.8–1831	221.75	-18.51	0.05	27.9	1.71 ± 0.15	6.1 ± 3.3	0.84
3FGL J1547.1–2801	236.81	-28.04	0.03	96.8	1.78 ± 0.10	19.0 ± 6.1	0.81
3FGL J1612.4–3100	243.10	-30.99	0.02	495.0	1.86 ± 0.08	38.0 ± 7.8	0.81
<b>3FGL J1714.1–2029</b>	258.52	-20.48	0.03	73.8	1.44 ± 0.12	5.1 ± 2.3	0.90
<b>3FGL J1711.6+8846</b>	258.67	88.75	0.04	44.3	1.83 ± 0.15	8.8 ± 4.2	0.90
3FGL J1824.4+4310	276.12	43.18	0.03	80.9	1.83 ± 0.15	13.6 ± 5.3	0.88
3FGL J1841.2+2910	280.36	29.16	0.02	195.9	1.80 ± 0.08	29.0 ± 7.1	0.80
3FGL J1855.1–6008	283.67	-60.13	0.06	21.4	1.84 ± 0.16	7.2 ± 3.9	0.84
3FGL J1908.8–0130	287.20	-1.53	0.02	306.4	1.52 ± 0.21	18.6 ± 2.8	0.82
<b>3FGL J1910.8+2855</b>	287.71	28.94	0.02	102.3	1.62 ± 0.10	9.8 ± 3.3	0.90
3FGL J1939.6–4925	294.96	-49.47	0.03	64.6	1.85 ± 0.11	14.9 ± 5.0	0.85
<b>3FGL J1944.1–4523</b>	296.11	-45.38	0.02	100.7	1.64 ± 0.10	9.4 ± 3.3	0.89
3FGL J1959.8–4725	299.94	-47.43	0.01	923.8	1.52 ± 0.08	30.5 ± 5.0	0.87
3FGL J2108.6–8619	316.99	-86.31	0.03	91.0	1.65 ± 0.12	10.3 ± 4.0	0.87
3FGL J2312.9–6923	348.40	-69.39	0.04	35.3	1.72 ± 0.17	5.5 ± 2.9	0.86
3FGL J2316.8–5209	349.28	-52.19	0.06	37.3	1.89 ± 0.16	10.8 ± 5.0	0.85
3FGL J2347.9+5436	356.97	54.58	0.02	163.0	1.79 ± 0.08	24.2 ± 6.4	0.82

**Table 2.** Same as Table 1 for UCS<sub>agn</sub> HSP candidates.

Source name	RA	DEC	pos <sub>68</sub> %	TS	Ph.Index	Flux	$L_{HSP}$
	[deg]	[deg]	[deg]			[ $10^{-9}$ ph/cm <sup>2</sup> /s]	
3FGL J0020.9+0323	5.26	3.36	0.04	60.7	2.01 ± 0.14	23.3 ± 8.4	0.88
3FGL J0049.0+4224	12.26	42.38	0.04	37.0	1.81 ± 0.16	8.1 ± 4.4	0.82
3FGL J0234.2-0629	38.59	-6.47	0.03	90.7	1.83 ± 0.11	15.6 ± 4.8	0.84
3FGL J0251.1-1829	42.79	-18.50	0.02	104.3	1.59 ± 0.10	7.0 ± 2.2	0.88
3FGL J0312.7-2222	48.15	-22.36	0.02	177.1	1.84 ± 0.08	22.3 ± 5.2	0.87
3FGL J0506.9+0321	76.71	3.38	0.03	77.1	1.81 ± 0.12	15.3 ± 6.0	0.89
3FGL J0524.5-6937	81.16	-69.61	0.03	94.1	2.05 ± 0.15	49.4 ± 21.2	0.86
3FGL J0527.3+6647	81.86	66.80	0.03	51.9	1.91 ± 0.15	13.0 ± 6.0	0.83
3FGL J0731.8-3010	112.96	-30.13	0.04	37.1	1.96 ± 0.17	22.4 ± 11.9	0.84
3FGL J0813.5-0356	123.45	-3.95	0.04	57.0	1.71 ± 0.12	9.1 ± 3.5	0.88
3FGL J0928.3-5255	142.09	-52.94	0.02	98.7	2.09 ± 0.09	88.0 ± 25.5	0.80
3FGL J0952.8+0711	148.22	7.23	0.04	51.0	1.92 ± 0.15	14.0 ± 6.0	0.84
3FGL J1057.6-4051	164.43	-40.87	0.03	40.2	1.72 ± 0.15	6.6 ± 3.4	0.82
3FGL J1155.3-1112	178.82	-11.19	0.03	52.5	2.03 ± 0.15	21.2 ± 8.9	0.89
3FGL J1222.7+7952	185.92	79.90	0.04	43.8	2.13 ± 0.22	21.1 ± 12.1	0.86
3FGL J1225.4-3448	186.35	-34.75	0.05	22.3	1.74 ± 0.19	5.1 ± 3.4	0.86
3FGL J1234.7-0437	188.71	-4.56	0.04	51.5	2.01 ± 0.14	23.5 ± 9.7	0.87
3FGL J1513.3-3719	228.35	-37.39	0.03	54.7	1.94 ± 0.13	19.8 ± 8.4	0.87
3FGL J1525.8-0834	231.53	-8.53	0.03	59.5	1.92 ± 0.12	20.0 ± 7.3	0.89
3FGL J1528.1-2904	232.12	-29.11	0.06	26.3	1.80 ± 0.18	8.7 ± 5.4	0.83
3FGL J1545.0-6641	236.21	-66.71	0.02	150.1	1.60 ± 0.10	11.2 ± 3.9	0.84
<b>3FGL J1549.9-3044</b>	237.46	-30.75	0.02	64.3	1.61 ± 0.12	6.2 ± 2.6	0.91
3FGL J1619.1+7538	244.78	75.61	0.02	107.1	1.87 ± 0.10	15.5 ± 4.7	0.88
3FGL J1922.2+2313	290.57	23.25	0.03	80.8	2.22 ± 0.14	93.1 ± 36.7	0.87
3FGL J2015.3-1431	303.81	-14.55	0.06	17.4	1.81 ± 0.21	5.6 ± 4.2	0.85
3FGL J2043.6+0001	310.94	0.00	0.04	48.5	2.02 ± 0.15	21.5 ± 8.1	0.87
3FGL J2053.9+2922	313.45	29.37	0.02	359.6	1.77 ± 0.06	46.0 ± 8.4	0.85
<b>3FGL J2142.6-2029</b>	325.66	-20.50	0.04	36.1	1.69 ± 0.17	5.0 ± 2.9	0.91
<b>3FGL J2145.5+1007</b>	326.38	10.13	0.03	34.1	1.70 ± 0.20	4.8 ± 3.4	0.90
3FGL J2224.4+0351	336.12	3.89	0.05	29.5	1.94 ± 0.18	13.2 ± 6.4	0.89
<b>3FGL J2300.0+4053</b>	345.06	40.88	0.03	52.5	1.64 ± 0.14	6.2 ± 3.0	0.90
3FGL J2309.0+5428	347.20	54.41	0.03	77.1	1.75 ± 0.10	16.2 ± 5.7	0.85
<b>3FGL J2321.6-1619</b>	350.40	-16.32	0.02	174.5	1.73 ± 0.08	17.3 ± 4.1	0.91

**Table 3.** Estimates of the maximum redshift values of the VHC sources for which the sources are still detectable at  $5\sigma$  in a 50 hours of current IACT and 50 (5) hours of CTA observations, respectively. If no value is given, the source will not be significantly detected within the assumed observation time. Sub- and superscript numbers give the change in the redshift values if the *Fermi*-LAT spectrum is extrapolated within  $1\sigma$  uncertainties. See main text for further details and caveats.

Source name	$T_{\text{obs}} = 50$ hours, current IACTs	$T_{\text{obs}} = 5$ hours, CTA	$T_{\text{obs}} = 50$ hours, CTA
BCU $HC_{TeV}$ candidates			
3FGL J0047.9+5447	$0.18_{-0.17}^{>0.50}$	$0.15_{-0.24}^{>0.50}$	$> 0.50_{-0.38}$
3FGL J1155.4-3417	$0.26_{-0.17}^{>0.50}$	$0.35_{-0.24}^{>0.50}$	$> 0.50$
3FGL J1434.6+6640	$0.15_{-0.13}^{+0.27}$	$0.14_{-0.15}^{+0.33}$	$> 0.50_{-0.31}$
3FGL J0921.0-2258	—	—	—
3FGL J0648.1+1606	$0.03_{-0.19}^{+0.19}$	$0.01_{-0.35}^{+0.19}$	$0.29_{-0.26}^{>0.50}$
3FGL J1711.6+8846	$0.04_{-0.28}^{+0.22}$	$0.02_{-0.35}^{+0.24}$	$0.32_{-0.29}^{>0.50}$
3FGL J1714.1-2029	$0.38_{-0.28}^{>0.50}$	$0.47_{-0.35}^{>0.50}$	$> 0.50$
3FGL J1910.8+2855	$0.18_{-0.15}^{+0.25}$	$0.16_{-0.15}^{+0.28}$	$> 0.50_{-0.17}$
3FGL J0153.4+7114	—	—	$0.43_{-0.50}^{>0.50}$
3FGL J0506.9-5435	$0.05_{-0.21}^{>0.50}$	$0.25_{-0.26}^{>0.50}$	$> 0.50_{-0.07}$
3FGL J1944.1-4523	$0.27_{-0.21}^{>0.50}$	$0.34_{-0.26}^{>0.50}$	$> 0.50_{-0.07}$
UCS <sub>agn</sub> $HC_{TeV}$ candidates			
3FGL J1549.9-3044	$0.13_{-0.15}^{+0.27}$	$0.15_{-0.20}^{>0.50}$	$> 0.50_{-0.29}$
3FGL J2142.6-2029	$0.05_{-0.15}^{+0.28}$	$0.07_{-0.20}^{+0.35}$	$0.41_{-0.35}^{>0.50}$
3FGL J2321.6-1619	$0.23_{-0.15}^{+0.20}$	$0.30_{-0.20}^{>0.50}$	$> 0.50$
3FGL J2145.5+1007	$0.04_{-0.32}^{+0.33}$	$0.02_{-0.35}^{+0.35}$	$0.26_{-0.37}^{>0.50}$
3FGL J2300.0+4053	$0.15_{-0.32}^{+0.32}$	$0.13_{-0.35}^{+0.35}$	$> 0.50_{-0.37}$